Contents lists available at ScienceDirect

Applied Catalysis B: Environmental

Influence of preparation method on dispersion of cobalt spinel over alumina extrudates and the catalyst deN$_2$O activity

Gabriela Grzybek [a],[*], Sylwia Wójcik [a], Klaudia Ciura [a], Joanna Gryboś [a], Paulina Indyka [a], Marcin Oszajca [a], Paweł Stelmachowski [a], Stefan Witkowski [a], Marek Inger [b], Marcin Wilk [b], Andrzej Kotarba [a], Zbigniew Sojka [a]

[a] Faculty of Chemistry, Jagiellonian University, Ingardena 3, 30-060, Krakow, Poland
[b] New Chemical Syntheses Institute, Al. Tysiąclecia Państwa Polskiego 13a, 24-110 Puławy, Poland

ARTICLE INFO

ABSTRACT

A series of supported catalysts of the Co$_3$O$_4$ spinel active phase dispersed over alumina extrudates (9 × 25 mm) was prepared by several methods (incipient wetness impregnation with Co(NO$_3$)$_2$ and CoCl$_2$, with glycerol-assisted impregnation with Co(NO$_3$)$_2$, combustion synthesis, and two variants of spray deposition with Co(NO$_3$)$_2$ on pristine and ammonia soaked extrudates). The catalysts were characterized by XRF, XRD, RS, UV–vis, SEM/TEM/EDX, and their catalytic deN$_2$O activity was investigated in the temperature programmed surface reaction (TPSR) mode. The relation between the spinel active phase particle size and its radial dispersion over the alumina extrudate and the deN$_2$O activity was revealed and quantified. For the assessment of the active phase utilization, the N$_2$O concentration profile across the extrudates was calculated using Thiele modulus and compared with the radial distribution of the spinel. It was shown that the dispersion of spinel active phase exhibits optimal profile when the sample is obtained in the presence of the organic components of the precursor mixture (glycerol or urea). The obtained results were discussed in the context of practical implications for the development of an efficient, low-cost catalyst for the N$_2$O abatement.

© 2017 Elsevier B.V. All rights reserved.

1. Introduction

Recent progress in the Earth's climate and atmosphere chemistry research recognized N$_2$O as one of the most dangerous greenhouse gasses, together with carbon dioxide and methane [1]. Despite the fact that the contribution of N$_2$O to the total greenhouse gas emissions is at the level of around 6%, due to its long lifetime in the atmosphere (∼150 years), the global warming potential of N$_2$O exceeds the corresponding values for CO$_2$ and CH$_4$ by 310 and 21 times, respectively [1]. N$_2$O is emitted from the natural environment and anthropogenic sources, with nitric and adipic acids plants belonging to the main industrial contributors [2].

In the particular case of nitric acid plants a large gamut of catalysts has been investigated in N$_2$O decomposition, such as simple and mixed oxides [3–6], spinels [7–9], perovskites [10–12], zeolites [13] as well as supported oxides [2,14–16]. Among them, one of the most active was found to be cobalt spinel, however, its insufficient mechanical stability in the form of extrudates and the high cost of cobalt limits its practical applications in the bulk form. These drawbacks may be, however, overcome by the simple dispersion of the spinel active phase over a cheap and mechanically robust carrier. Indeed, there are several reports in the literature concerning dispersion of the cobalt spinel on alumina [17], ceria [2], titania [18] or even on metallic monoliths [19].

The deposition of the active phase on the support is a critical issue for the development of a catalyst with a satisfactory performance. Among many available preparation techniques for the practical applications, simple, reproducible and easily scalable are preferred at the industrial scale. The most popular one is the impregnation method using an aqueous solution of the active phase precursors [20–22]. It has been recently shown that the slight modification by performing glycerol-assisted impregnation can lead to the improvement of the catalyst performance, achieved by increasing the cobalt spinel dispersion on the alumina support and favorable faceting of the Co$_3$O$_4$ nanocrystals [17]. The spray deposition, combustion synthesis, and precipitation were also used to prepare supported catalysts [23]. However, until now, there is

Nomenclature

Symbols

η	Effectiveness factor
$C_{N2O,s}$	N$_2$O concentration on the external surface of the catalyst
C_{N2O}	N$_2$O concentration on the catalyst surface
D_m	Molecular diffusivity, m^2 s^{-1}
D_{eff}	Effective diffusion coefficient, m^2 s^{-1}
D_{ij}	Binary molecular diffusion coefficient, m^2 s
D_k, $D_{k,N2O}$	Knudsen diffusivity, m^2 s^{-1}
M_i, M_j, M_{N2O}	Molar weight, g mol^{-1}
P	Pressure, Pa
y_i, y_j	Molar fraction
D	Diffusivity, m^2 s^{-1}
F	External surface area of catalyst particle, m^2
k	Kinetic rate constant, m^3 kg^{-1} s^{-1}
q	Porous tortuosity
r	Distance from the center of the catalyst particle, m
r_o	Catalyst pore radius, m
r_p	Catalyst particle radius, m
V	Catalyst particle volume, m^3
ε	Porosity of catalyst particle
ρ_c	Density of catalyst bed, kg m^{-3}
ρ_b	Apparent density (bulk) kg m^{-3}

no systematic study on rational selection of the optimal support nature, dispersion method and calcination conditions for manufacturing of the supported cobalt spinel catalyst for high performance in the N$_2$O decomposition.

The aim of this work is to evaluate several preparation methods for optimal dispersion of cobalt spinel on alumina extrudates in the context of the development of cheap industrial catalyst based on Co$_3$O$_4$|Al$_2$O$_3$ formulation with high activity in the decomposition of nitrous oxide from tail gasses of nitric acid plants.

2. Experimental part

2.1. Catalyst preparation

Alumina support extrudates (9×25 mm) prepared from commercial powder pseudoboehmite (Sasol Versal) by calcination at 1000 °C for 4 h were supplied by the Institute of New Chemical Syntheses (INS Pulawy, Poland). The spinel active phase was deposited onto the alumina support ($S_{BET} = 100$ m^2 g^{-1}) by the following methods: incipient wetness impregnation method (aqueous solution of Co(NO$_3$)$_2$ or CoCl$_2$), glycerol-assisted impregnation method [17] (30 vol.% of glycerol in aqueous solution of Co(NO$_3$)$_2$), two variants of spray deposition (from Co(NO$_3$)$_2$ precursor spread on pristine extrudates or on extrudates soaked with NH$_3$ prior the spreading) as well as combustion synthesis method (using Co(NO$_3$)$_2$ and urea as a fuel) [24–26]. All samples were dried at 120 °C for 12 h and then calcined at 600 °C for 4 h. The labeling of the samples together with the synthesis parameters and cobalt loading determined from XRF analysis are shown in Table 1. We have selected cobalt nitrates and chlorides as precursors for the catalyst preparation since they are easily soluble in water and readily available. Taking into account the aim of industrial application of the developed catalyst, the price of the precursors was also an important issue.

2.2. Catalysts characterization

The structure and polymorphic composition of the alumina support was thoroughly examined by X-ray powder diffraction measurements, which were carried out by means of a Bruker D8-Advance instrument with the CuKα radiation ($\lambda = 1.540598$ Å) in the 2 theta range between 10° and 80° with the step of 0.02° and a time of 3 s per step. The XRD patterns were analyzed quantitatively by Rietveld method using Maud software [27]. Prior to the analysis, the amorphous background was removed from the experimental diffractogram.

The cobalt loading in the extrudates was determined by means of energy-dispersive XRF spectrometer (Thermo Scientific, ARL QUANT'X). The X-ray radiation was generated with a Rh anode (4–50 kV with 1 kV step), 1 mm size beam and a 3.5 mm Si(Li) drifted crystal detector with a Peltier cooling ∼185 K were used. For the quantitative analysis, a UniQuant software along with a series of the calibration metallic standards was employed.

The presence of the spinel structure was confirmed by the micro-Raman spectroscopy (μ-RS) investigations. The measurements were carried out at the wavelength excitation of 514 and 785 nm (100–1000 cm^{-1}, 1 cm^{-1} resolution) and recorded at room temperature using a Renishaw InVia spectrometer and a confocal Leica DMLM microscope equipped with a CCD detector. The signal to noise ratio was optimized by accumulating at least nine scans for each measurement.

The catalyst samples were also investigated by the optical diffuse reflectance UV–vis (DRS) spectroscopy. The spectra were collected with a Perkin Elmer Lambda 12 spectrometer in the range of 200–900 nm at ambient conditions. As a distribution reference and a dilution medium BaSO$_4$ was used.

Morphology and local chemical composition of the supported catalyst were examined by the scanning and transmission electron microscopies (SEM and TEM). The SEM observations were carried out by TESCAN Vega 3 LUM (20 keV) electron microscope after coating with gold. Additionally, in order to analyze the spatial distribution and speciation of cobalt species, a linear scan of the chemical composition for each extrudate was performed.

Transmission electron microscopy measurements were carried out using a Tecnai Osiris instrument (FEI) with the X-FEG Schottky field emitter operated at accelerating voltage of 200 kV. Structural analysis was performed using TEM images and selected area electron diffraction (SAED) patterns. The Z-contrast imaging was carried out using a high angle annular dark field (HAADF) detector in the scanning mode. Spatially resolved information about the element repartition was obtained using a Super-X EDX (Energy Dispersive X-ray) windowless detector system with a 4-sector silicon drift detector (SDD). The samples for the TEM characterization were scraped from the extrudates, crushed and spread on lacey carbon-coated copper grids.

2.3. N$_2$O decomposition tests

The catalytic activity tests in the deN$_2$O reaction were carried out in a temperature programmed surface reaction (TPSR) mode (10 K min^{-1}) in a quartz flow reactor. The measurements were performed using a 300 mg of crushed samples (sieve fraction of 0.2–0.3 mm) and the flow of 5% N$_2$O in He, 30 ml min^{-1} (GHSV = 7 000 h^{-1}), at the atmospheric pressure. The reaction was monitored continuously by analyzing the gaseous reactants with a quadrupole mass spectrometer (RGA200, SRS, lines with m/z = 44 (N$_2$O), 32 (O$_2$), 30 (NO), 28 (N$_2$), 18 (H$_2$O)). To ensure that the reactor is operating in the kinetic regime, the criterial numbers for extra- and intragranular diffusion limitations were checked according to the Eurokin procedure [28]. The Peíclet number (Pe ∼ 0.005) and Damköhler number (Dk ∼ 0.1) indicated that practically a perfect

Table 1
The catalysts synthesis parameters and cobalt content (determined from XRF measurements).

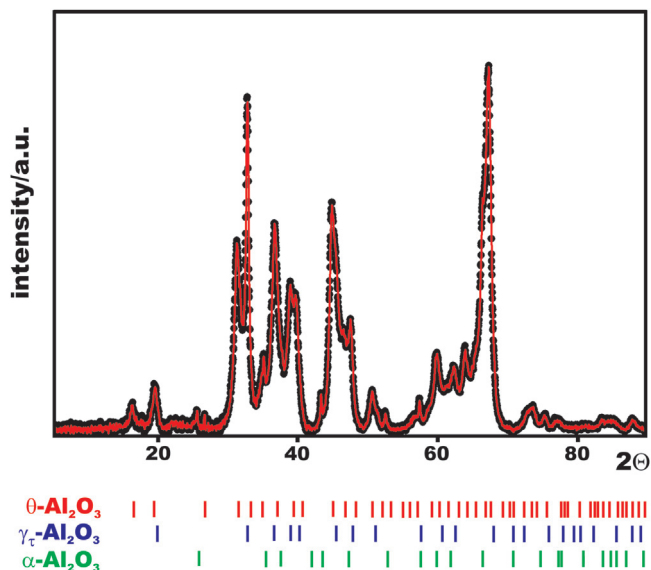| Catalyst	Synthesis method	Cobalt wt.%
Im-N	impregnation with 1.2 M $Co(NO_3)_2$ aqueous solution	6.4
Im-Cl	impregnation with 1.2 M $CoCl_2$ aqueous solution	3.4
Im-Gl	impregnation with 1.2 M $Co(NO_3)_2$ 30% glycerol-water solution	4.2
Cm-N	combustion synthesis using urea as a fuel	3.0
Sp-N	spray deposition of 2 M $Co(NO_3)_2$ aqueous solution on the pristine Al_2O_3 extrudate	2.8
Sp-NN	spray deposition of 2 M $Co(NO_3)_2$ aqueous solution on Al_2O_3 extrudates soaked with NH_3 (25%, 2 h)	1.4

Fig. 1. The XDR pattern (black dots) of the bare alumina support with the quantitative Rietveld refinement of the phase composition (red line). Red, blue and green sticks show the positions of (hkl) reflections for theta alumina (θ-Al_2O_3), tetragonal gamma alumina (γ-Al_2O_3) and alpha alumina (α-Al_2O_3), respectively. (For interpretation of the references to colour in this figure legend, the reader is referred to the web version of this article.).

mixing regime was achieved for all the measurements [29]. This assumption was additionally confirmed by the results of reactor modeling described by Zielinski in [30], which shows that at such conditions and for these criterial numbers the concentration of reactants is practically uniform in the whole reactor volume.

3. Results and discussion

3.1. Al_2O_3 support characterization

The shape of an alumina extrudate used as a support for cobalt spinel active phase can be represented by a cylinder of the diameter and length of 9 mm and 25 mm, respectively. Our previous work has shown that the internal macroporosity of the alumina extrudate consists of a network of pores in the range of 3–50 μm. They are preferentially aligned along the main axis of the extrudate. The total volume of the macropores available for aqueous solution filling was equal to 0.42 cm^3 g^{-1}. Additionally, the water porosity of 0.75 ml g^{-1} of the support was determined [17].

The phase composition of the alumina support used for the preparation of the cobalt spinel catalyst was determined by a Rietveld analysis, taking into account fifteen possible different phases of alumina. For each phase, theoretical powder pattern was simulated, based on the structure of its unit cell. By comparing the theoretical powder patterns with the experimental data three phases: theta alumina (θ-Al_2O_3), tetragonal gamma alumina (γ_t-Al_2O_3) and alpha alumina (α-Al_2O_3) were identified as contributing to the obtained XRD patterns (Fig. 1). The experimental data (black

dots) agree well with the simulated pattern (red line). Red, blue and green vertical lines indicate the positions of the (hkl) reflections characteristic for theta, tetragonal gamma and alpha alumina, respectively. According to the Rietveld refinement of the XRD data, the alumina support has the following phase composition: θ-Al_2O_3: 51.4 ± 0.0%, γ_t-Al_2O_3: 47.3 ± 2.1% and α-Al_2O_3: 1.3 ± 0.1%.

3.2. Catalysts characterization

The synthesized catalysts were thoroughly characterized with respect to their chemical and phase composition, morphology and texture by spectroscopic and microscopic techniques. The content of cobalt in the resultant supported catalysts based on XRF analysis is presented in Table 1. It should be noticed, that the amount of the cobalt phases depends strongly on the applied synthesis method, ranging from 1.9 to 6.4 wt.% of Co_3O_4. The loading of cobalt spinel obtained using both spray methods is significantly lower than in the case of all the impregnation methods and the combustion synthesis as well.

The crystalline structure of the prepared catalyst was examined by μ-Raman spectroscopy. Raman spectra of the investigated samples recorded with an excitation wavelength of 785 nm are collated in Fig. 2, together with the cross-sections of the catalyst extrudates showing the probed areas (marked with arrows). Five bands typical of the cubic cobalt spinel structure located at 195 (F_{2g}), 487 (E_g), 526 (F_{2g}), 624 (F_{2g}) and 694 (A_{1g}) cm^{-1}, were observed for all catalysts, confirming the presence of a nanocrystalline spinel [31–33]. The difference in homogeneity of spinel distribution can be clearly noticed by analyzing the signal intensity changes while moving along the extrudate radius. For the sample obtained by the incipient wetness impregnation with $Co(NO_3)_2$ a uniform radial distribution of Co_3O_4, visible also in the corresponding picture, was observed. The incipient wetness impregnation with $CoCl_2$ in turn, resulted in two-colored cross-section (black at the edge and blue inside the pellet, Im-Cl sample), suggesting the presence of two different cobalt spinels: black Co_3O_4 and blue $CoAl_2O_4$ (see below). In the middle of the pellet, no spinel phase was detected. In the case of the Im-Gl sample obtained by the glycerol-assisted incipient wetness impregnation with $Co(NO_3)_2$, a fairly uniform distribution of Co_3O_4 over the whole cross-section of the extrudate was observed. Only in the center of the pellet the blue phase can be perceived, for which the Raman spectra exhibits very low intensity, implying a low concentration of the spinel phase. For the catalyst obtained by means of the combustion synthesis (Cm-N), the spinel phase was detected along the whole cross-section of the catalyst. Yet, the observed difference in the peak intensities in the Raman spectra from different spots indicates the decrease of the cobalt concentration while going inside the cross-section, reflected in the corresponding changes in the intensity of the black shade across the pellet. In this sample, no blue coloration was observed suggesting the presence of the Co_3O_4 spinel only. Both of the spray methods lead to the appearance of very uneven distribution of cobalt, as it can be inferred from the presence of the clear core (white) and shell (dark) morphology. The Raman spectra of the spinel were observed only for the shell part, while essentially no μ-RS signal was observed for the white core. It means that these methods lead to a limited penetration of
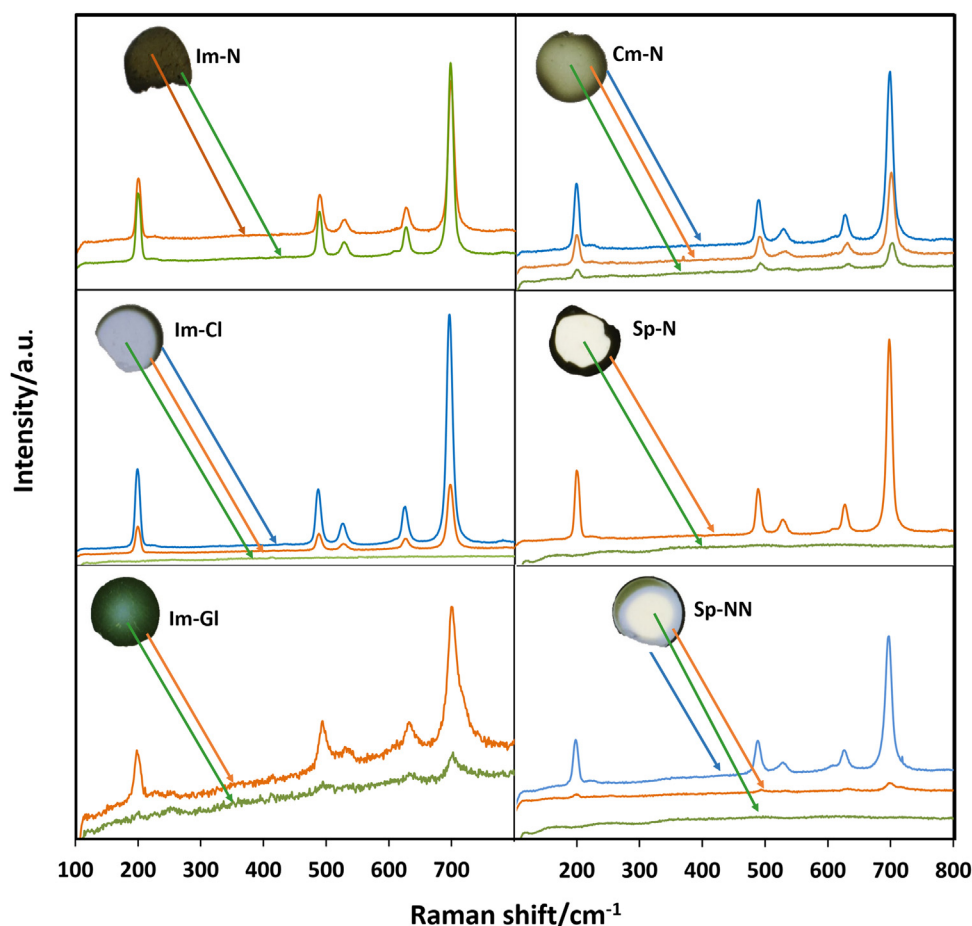
Fig. 2. Raman spectra of prepared catalysts registered with an excitation wavelength of 785 nm for the Im-N, Im-Cl, Im-Gl, Cm-N, Sp-N and Sp-NN samples. The spectra were registered at various regions of the cross-section of the catalyst extrudates (see inserted images) that are indicated with arrows.

the alumina support extrudate by the cobalt precursor solution. Immersing the support extrudate in ammonia solution prior the spraying with $Co(NO_3)_2$ modified the shell morphology (sample Sp-NN), which then consisted of two phases – wide blue ring due to $CoAl_2O_4$ that is surrounded by a thin dark layer of Co_3O_4.

Although two colors imply the presence of Co_3O_4 (dark) and $CoAl_2O_4$ (Thenard blue) this fact is not appreciably reflected in the Raman spectra recorded with the laser line of 785 nm (Fig. 2). In order to prove their chemical nature, the optical diffuse reflectance spectra for the investigated samples were next recorded. The obtained results together with the reference spectra of the Co_3O_4 and $CoAl_2O_4$ spinels are presented in Fig. 3. For the Im-N, Sp-N samples the results are in-line with the μ-Raman analysis. In these cases, only the typical spectra of the cobalt spinel are observed [34–36]. The broad absorption at 1.6–1.9 eV is assigned to the overlapping signals due to the $t_{2g}(Co^{3+}) \rightarrow t_2(Co^{2+})$ charge transfer (1.65 eV) and the $^1A_1 \rightarrow {}^1T_1$ d–d transition in the low spin octahedral Co^{3+} ions. A broad absorption in the range of 2.3–2.9 eV can arise from the $p(O^{2-}) \rightarrow t_2(Co^{2+})$ LMCT transition at about 2.4 eV and the $p(O^{2-}) \rightarrow e_g(Co^{3+})$ LMCT transition at about 2.8 eV [36,37]. In an alternative interpretation proposed elsewhere [38], this triplet is associated with the splitting of the $^4A_2(F) \rightarrow {}^4T_1(P)$ band due to the Jahn–Teller distortion of the tetrahedral Co^{2+} ions. The presence of this spectrum evidently indicates the Thenard blue as a responsible for the blue color in the samples Im-Cl and Sp-NN. Additionally, for some samples (Im-Cl, Im-Gl, Cm-N and Sp-NN) the combination of spectra described above is observed due to a partial substitution of Al^{3+} for Co^{3+}. For the rest of the samples, depending on the analyzed region in the extrudate cross-section, different

spectra were recorded. The spectra characteristic of Co_3O_4 were observed for the Im-Gl, Cm-N, Sp-N and Sp-NN catalysts, whereas the typical UV–vis spectra of $CoAl_2O_4$ were registered for the blue part of the Im-Cl and Sp-NN samples.

The formation of the Thenard blue in the case of the Im-Cl, Im-Gl and Sp-NN samples was next corroborated by additional μ-Raman Spectroscopy measurements, using an excitation wavelength of 514 nm. The Raman spectra recorded in a narrow scan mode around A_{1g} region are presented in Fig. 4. For all samples, splitting of the A_{1g} band confirms the presence of partial substitution of the octahedral Co^{3+} cations by Al^{3+}. For the sake of clarity, we have explicitly deconvoluted the A_{1g} peak into the two components with the maxima located at $655.5\,cm^{-1}$ and $683.7\,cm^{-1}$ for the Im-Cl sample, $647.2\,cm^{-1}$ and $682.1\,cm^{-1}$ for the Im-Gl sample and $662.4\,cm^{-1}$ and $679.0\,cm^{-1}$ for the Sp-NN sample. The signals that appeared at high wavenumber of the A_{1g} band are associated with the octahedral Al^{3+} ions that substituted Co^{3+} ions in the spinel framework. The small shifts, can be associated with a particle size effect [39] and/or thermal effect induced by the local overheating by laser irradiation, which are often discussed in terms of Gruneisen model [40]. More detailed account for this issue has been published by us previously [34].

In addition, we performed the TPR measurements for the Im-Cl sample with the maximum amount of the $CoAl_2O_4$ phase and compared the results with the reduction profile for a reference $Co_3O_4|Al_2O_3$ sample containing only cobalt spinel nanocrystals dispersed on the alumina surface. The obtained profiles (Fig. S1 in the supporting information) are featured by the presence of two reduction peaks in the case of the $Co_3O_4|Al_2O_3$ sample assigned
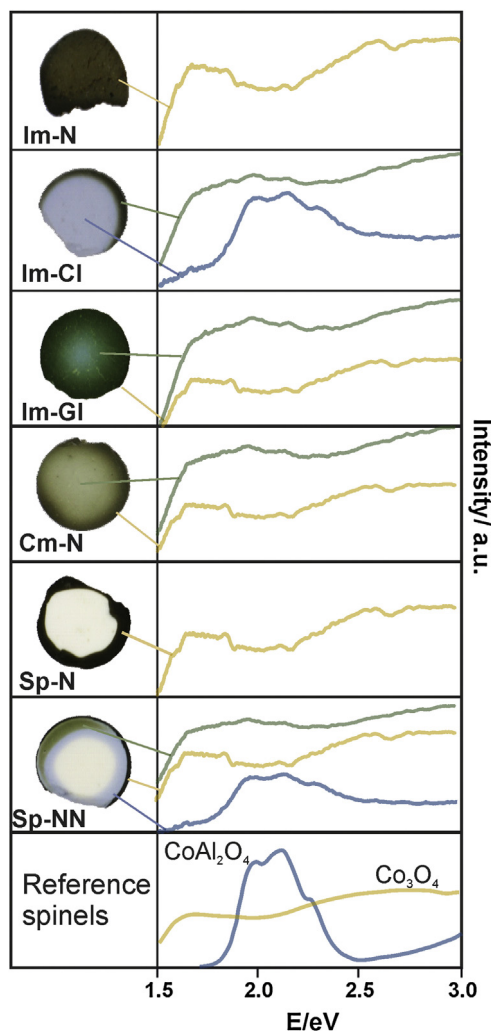
Fig. 3. The optical diffuse reflectance spectra converted to absorption for the Im-N, Im-Cl, Im-Gl, Sp-N and Sp-NN catalysts, together with the reference spectra of Co_3O_4 and $CoAl_2O_4$ (in the bottom).

Fig. 4. Narrow range Raman spectra of the A_{1g} band for the core and shell of the Im-Cl, Im-Gl and Sp-N catalysts registered at the excitation wavelength of 514 nm.

to reduction of Co^{3+} to Co^{2+} and Co^{2+} to Co^0, whereas the broad reduction maximum observed for the Im-Cl sample corresponds to reduction of Co^{2+} in the cobalt aluminate matrix, confirming the reported UV–vis and μ-RS results.

The results of SEM observations for all the investigated samples are collected in Fig. 5, where a_1-f_1 panels correspond to the secondary electrons (SE) images of the extrudates, a_2-f_2 panels show the spatial distribution of cobalt and a_3-f_3 panels show the line scan analysis. The resultant Co concentration profiles obtained by the least square fitting revealed changes in the amount of the deposited Co across the extrudate depending on the preparation method. As expected, for each sample the alumina content was essentially constant, therefore the corresponding Al-maps were omitted herein.

In the case of the Im-N extrudate (Fig. 5a_1, a_2) the EDX map shows a homogenous radial distribution of the Co species across the sample. Such distribution is in-line with the presence of cobalt exclusively in the form of Co_3O_4, implying that the cobalt(II) nitrate precursor penetrated the whole extrudate in a uniform way, as clearly confirmed by a more accurate linear scan results (Fig. 5a_3). The SEM analysis for the Im-Cl catalyst (Fig. 5b_1–b_2) shows a linear decrease of the Co amount upon passing from the edge to the center of the extrudate. It may be accounted for by a nonhomogeneous penetration of the cobalt chloride and the presence of two different forms of cobalt: Co_3O_4 in the region of higher Co amount (dark
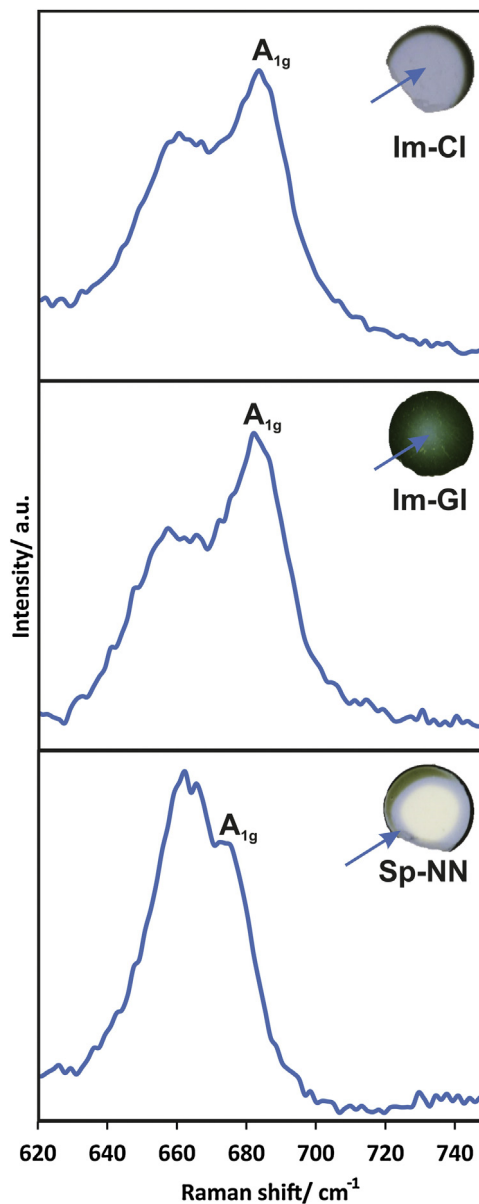
edge) and $CoAl_2O_4$ in the interior (blue region) of the extrudate. The SEM/EDX results agree well with the XRD, Raman and UV–vis data. Similar linear profile for cobalt distribution was observed in the case of the Im-Gl extrudate obtained by the glycerol-assisted impregnation (Fig. 5c_1, c_2). However, the smaller slope implies a more homogeneous distribution of cobalt. Contrary to the previous sample, the Im-Gl extrudate is lacking sharp color changes across the sample. The observed color intensity gradient, darker at the edge and brighter in the center suggests a more homogeneous penetration of Co precursor when the glycerol is present.

The combustion synthesis (Cm-N extrudate, Fig. 5d_1), in turn, leads to an enhanced cobalt concentration in the external region of the extrudate as revealed by the curved profile of Co radial distribution (Fig. 5d_3). In the case of the samples prepared by spray deposition on the pristine (Fig. 5e_1) and ammonia-soaked alumina extrudate (Fig. 5f_1), the resultant Co concentration profiles changed abruptly revealing highly uneven spreading of the cobalt spinel. For the Sp-N sample, the active Co_3O_4 phase is largely concentrated within the outer region of ∼1 mm, whereas the inert part of the
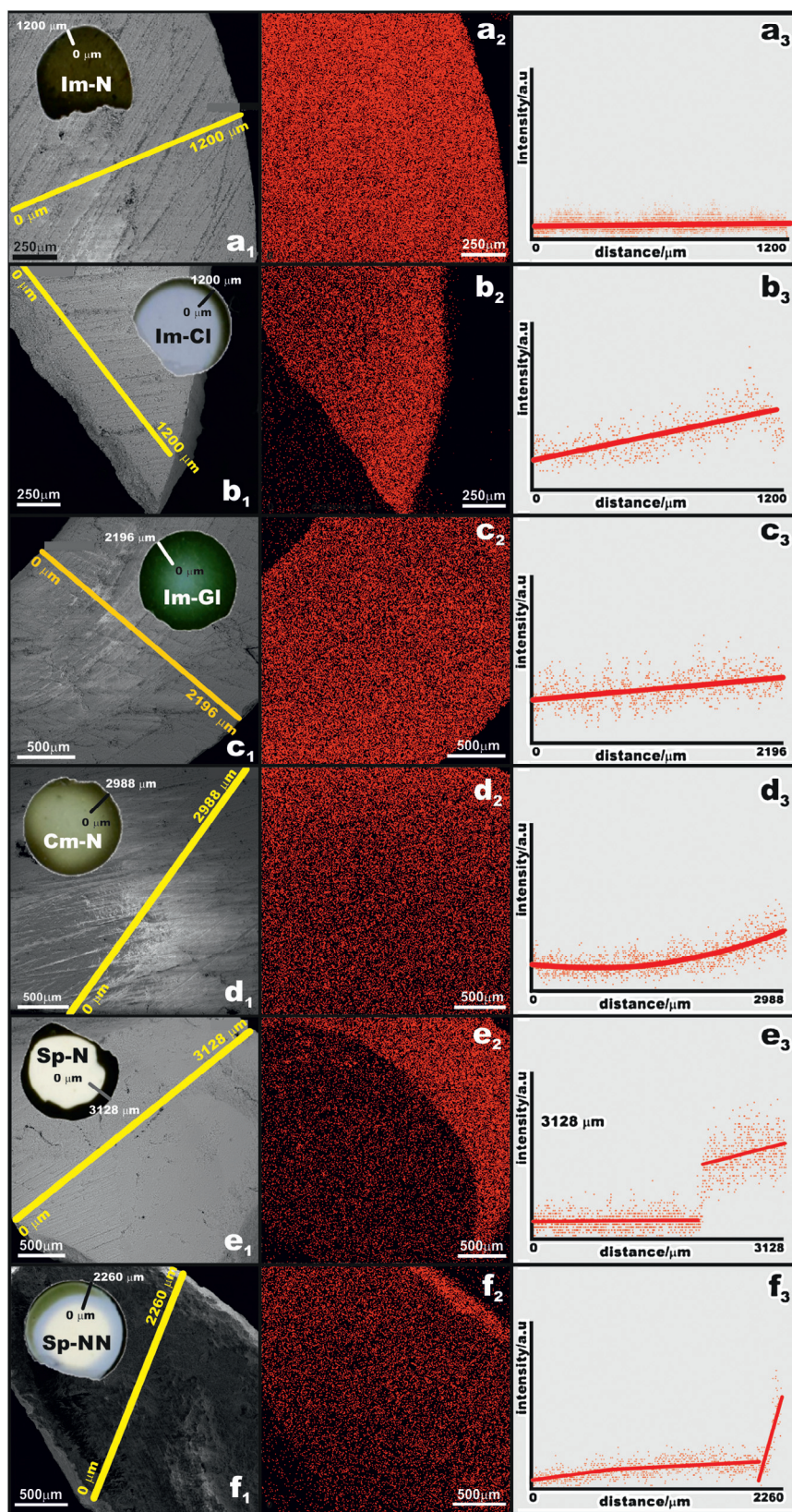
Fig. 5. Macrophotographic and SEM images of the extrudate cross-section of the catalysts obtained by various preparation methods (a_1-f_1), together with the Co elemental mapping (a_2–f_2) and the radial profile of the Co concentrations across the extrudate (a_3–f_3). The yellow line marks a linear EDX scan of the specimen. (For interpretation of the references to colour in this figure legend, the reader is referred to the web version of this article.)
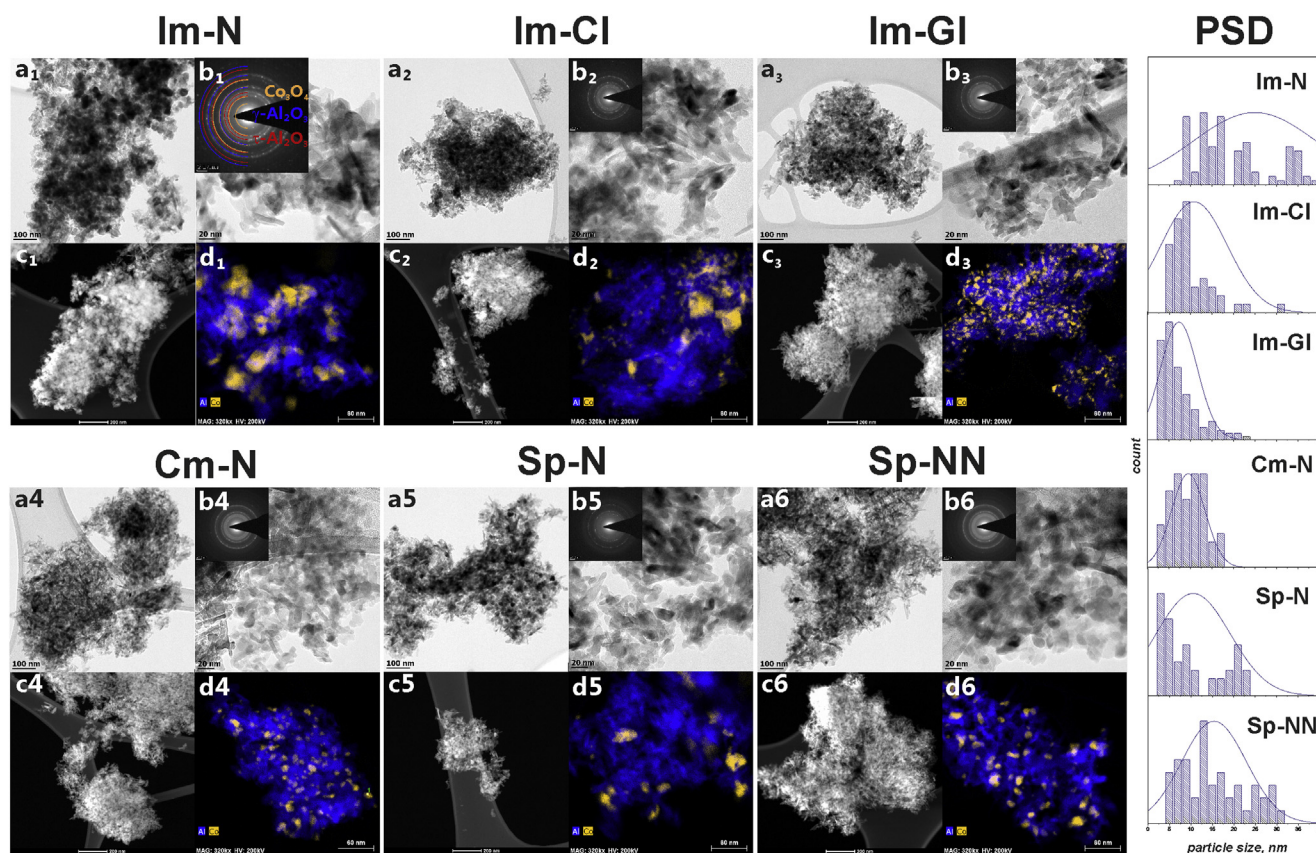
Fig. 6. TEM images (a–b) together with polycrystalline electron diffraction patterns of the Co_3O_4 spinel dispersed on the alumina support (b-insert), overview STEM-HAADF image (c) along with detail EDX map (d) of the Co (yellow) and Al (blue) distributions for the Im-N, Im-Cl, Im-Gl, Cm-N, Sp-N and Sp-NN samples. The right panel shows the corresponding particle size distributions (PSD) histograms and mono-modal profiles (solid line). (For interpretation of the references to colour in this figure legend, the reader is referred to the web version of this article.)

extrudate remains intact (Fig. 5e$_2$,e$_3$). Again, the result of the SEM-EDX analysis complement well the XRD and Raman spectroscopy results, showing the formation of the Co_3O_4 spinel only in the outer layer.

The extrudate Sp-NN (Fig. 5f$_1$,f$_2$) shows three regions of the cobalt radial distribution. As revealed in the linear scan (Fig. 5f$_3$) starting from the edge, the Co content dramatically decreases within 50 μm distance from the extrudate surface, then upon passing to the center, the changes are very small. The μ-RS results imply that the observed regions may be associated with the presence of cobalt in the form of the Co_3O_4 (dark) and $CoAl_2O_4$ (pale blue) spinels or their mixture (green).

TEM and STEM-HAADF images presented in Fig. 6(a–c) show the morphology of the Co_3O_4 spinel active phase dispersed on the alumina support. In all of the examined samples, the Co_3O_4 spinel was nanocrystalline, with the size distinctly smaller than the alumina crystals (except the Im-Gl, where the sizes of both phases were comparable). The Debye-Scherrer rings, presented in the selected area electron diffraction patterns were consistently indexed as those of the cubic Co_3O_4, θ-Al_2O_3, and tetragonal γ-Al_2O_3 phases (Fig. 6b$_1$–b$_6$ inserts). An example of the phase composition analysis is shown in Fig. 6b1-insert, where the observed ring reflections can be well assigned to Co_3O_4 (yellow), θ-Al_2O_3 (red) and γ$_T$-Al_2O_3 (blue).

As seen in Fig. 6(a–c) the majority of the investigated spinel nanoparticles retained equant polyhedral-shape morphology, while the shape of the Al_2O_3 crystallites was elongated and rather irregular. Differences in the local homogeneity of the spinel distribution were revealed by the EDX analysis (Fig. 6d$_1$–d$_6$). Statistically, the smallest size of cobalt spinel nanocrystals was observed

for the Im-Gl sample (7.3 nm ± 4.3 nm), where the tendency of the Co_3O_4 phase for successful decoration and uniform spreading over the Al_2O_3 phase is clearly visible. A slightly bigger size of the Co_3O_4 nanocrystals can be noticed for the Cm-N sample (9.4 nm ± 3.9 nm) with the size distribution well approximated with a Gaussian profile (Fig. 6, right panel). For the Im-Cl sample, a large variation of size and shape of the Co_3O_4 particles ranging from 10 to 50 nm can be seen, with a tendency to octahedral crystal morphology. In the case of the Im-N sample, aggregates of the spinel crystals with a diameter of about 25–30 nm, blended into the alumina grains were observed. For the Sp-N and Sp-NN samples obtained by spray method, a non-gaussian size distribution with two-modal profile was noticed (of about 5 and 20 nm and 10 with 25 nm, respectively), however, with a much narrower distribution profile than for the Im-N catalyst. Summarizing, the obtained results revealed that the synthesis conditions of the $Co_3O_4|Al_2O_3$ catalyst play a crucial role for both the particle size of the active phase and its spreading over the support. As shown in the particle size distributions (PSD) histograms (Fig. 6, right panel), the best dispersion and the smaller particle size were obtained for the catalysts prepared by the glycerol-assisted impregnation (Im-Gl) and the combustion synthesis (Cm-N).

The observed influence of the cobalt precursors and the presence of auxiliary organic molecules on the dispersion of cobalt species is a function of several parameters such as support wettability by the precursor solution, penetration of the support porosity by the precursor solution or a specific mechanism of the precursor decomposition (see supporting information S2). In particular, the effect of glycerol can be accounted for by the complexation of cobalt, leading to the formation of an intrapore cobalt glycerolate,
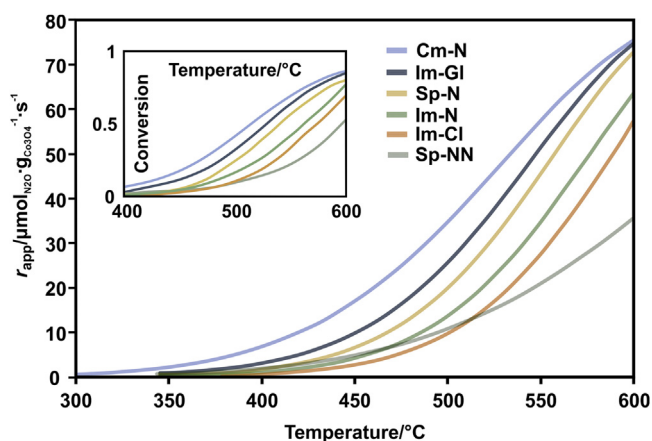
Fig. 7. The influence of the preparation method on the catalytic activity of $Co_3O_4|Al_2O_3$ catalyst presented as an apparent reaction rate at 550 °C together with the conversion curves (insert) as a function of temperature.

which upon calcination is transformed into well dispersed Co_3O_4 cubic nanocrystals of uniform particle size distribution. In the presence of organic compounds, calcination of the sample prepared from nitrate precursor leads to a space confined combustion-like synthesis, similar to that observed for urea addition (Cm-N). Both methods give rise to the uniform dispersion of the cobalt spinel particle size (Fig. 6). In the case of impregnation using the nitrate precursor only (Im-N), the formation of spinel nanoparticles occurs by dehydration and thermal decomposition of the deposited cobalt nitrate produced during drying. The latter process, due to the capillary effects is poorly controllable and is featured by high inherent heterogeneity. As a result, the catalysts prepared by this method exhibit the broadest and irregular particle size distribution profile. Similar broad profiles were obtained also in the case of the spray deposition method. As a result, three generic types of the spinel dispersion profiles can be distinguished: gradient (Cm-N, Im-Gl), uniform (Im-N) and core and shell (Sp-N, Sp-NN, Im-Cl).

3.3. Catalytic N_2O decomposition tests using powder samples

The impact of the catalyst morphology on the catalytic performance was directly probed by the N_2O decomposition reaction. For these tests, the powder samples obtained by crushing of the catalyst extrudates were used. Typical deN$_2$O results are shown in Fig. 7, where the experimental data are expressed as N_2O conversion (X_{N2O}) versus temperature (insert). In order to analyze the effect of the cobalt spinel loading on the catalytic activity, an apparent reaction rate (r_{app}, the number of N_2O molecules in μmol decomposed over 1 g of Co_3O_4 during one second) for all the catalysts was calculated. The differences in the catalyst preparation method cause a strong variation in the catalytic activity, which increases in the order: Sp-NN < Im-Cl < Im-N < Sp-N < Im-Gl < Cm-N. Thus, the samples exhibiting larger particle size (30–50 nm) of cobalt spinel (Sp-NN, Im-Cl, Im-N) are less active than the Sp-N, Im-Gl, Cm-N catalysts, which are characterized by the smaller particle size

(7–11 nm). However, the small size of cobalt spinel nanocrystals facilitates the solid-state reaction between the cobalt spinel and the alumina support. As a consequence, an inactive phase of $CoAl_2O_4$ spinel (Thenard blue) is formed. Thus, the lower activity of the Im-Gl catalyst with the smallest cobalt spinel crystals in comparison to the Cm-N catalyst can be associated with a higher extent of the Thenard blue formation.

The kinetic parameters such as apparent rate constants (k_{app}) at 550 °C and apparent activation energy (E_{app}) of N_2O decomposition were derived assuming the pseudo first order kinetics. The values of the calculated k_{app} and E_{app} are summarized in Table 2, together with the half conversion temperature ($T_{50\%}$), conversion at 550 °C (X_{550}) and apparent reaction rate at 550 °C (r_{app550}). The temperature of 550 °C was selected for kinetic parameters determination due to the fact, that all the catalysts exhibit reliably measurable activity at this temperature (Fig. 7). The determined values of E_{app} and k_{app} are in good agreement with the parameters published for the cobalt spinel previously [5].

The highest activity of the combustion synthesized Cm-N sample can arise from the uniform dispersion of cobalt spinel active phase, determined from TEM observations, as well as the absence of the parasitic $CoAl_2O_4$ of much lower activity [34]. Indeed, the least active Sp-NN and Im-Cl catalysts are featured by the extensive formation of the Thenard blue (see Figs. 2–4), and large agglomerated Co_3O_4 particles (Fig. 6). The kinetic parameters derived from the powder laboratory deN$_2$O catalytic tests were next used for assessment of the catalyst performance in the form of extrudates. In the particular case of N_2O decomposition, where the reaction ($N_2O_{(g)} \rightarrow O_{surf} + N_{2(g)}$) is essentially irreversible, the observed reaction rate constant corresponds to the intrinsic rate constant with a good approximation. The kinetic data determined from the powder catalyst studies were next used to predict the effectiveness factor for the extrudates.

3.4. Modeling of the diffusion resistance effect on the N_2O decomposition for the catalyst extrudates

In order to evaluate the effect of a diffusion resistance on the N_2O decomposition, the effectiveness factor, η, caused by the diffusion processes inside the extrudate bulk, was calculated.

The effectiveness factor is a function of the Thiele modulus, Φ,

$$\eta = \frac{1}{\Phi} \cdot \tanh(\Phi) \qquad (1)$$

The latter was calculated as:

$$\Phi = \frac{V}{F} \sqrt{\frac{k\varrho_c}{D_{eff}}} \qquad (2)$$

where: F – external surface area of catalyst particle m^2; V – catalyst particle volume, m^3, k – reaction rate constant, m^3 kg^{-1} s^{-1}.

The effective diffusion coefficient D_{eff} depends on the molecular (D_m) and Knudsen diffusion (D_k) coefficients:

$$D_{eff} = \varepsilon/q \left[\frac{1}{D_m} + \frac{1}{D_k} \right]^{-1} \qquad (3)$$

Table 2
The apparent kinetic parameters for N_2O decomposition for all the investigated catalysts tested in the powder form.

Catalyst	X_{550}	$T_{50\%}$	r_{app550} /μmolN$_2$O g$_{Co3O4}^{-1}$ s^{-1}	k_{app550}/s^{-1}	E_{app}/kJ mol^{-1}
Im-N	0.40	563	35.0	1.31	102
Im-Cl	0.34	579	27.1	0.94	111
Im-Gl	0.62	531	51.5	2.39	99
Cm-N	0.70	513	57.3	3.04	83
Sp-N	0.56	541	44.8	1.98	108
Sp-NN	0.19	596	21.0	0.72	119

Table 3
Summary of the basic textural characteristics of the alumina support.

S_{BET}/m^2 g^{-1}	ρ_b/g cm^{-3}	ε/%	r_o/nm	q	$d_{extrudate}$/mm	$d_{extrudate}$/mm after calcination	L/mm	ρ_c/g cm^{-3}
100	1.03	69	10	15	9	7.6	25	0.67

Table 4
Diffusion coefficients of N$_2$O at various temperatures.

T/°C	600	550	500	450
D_m/m^2 s^{-1}	9.97·10^{-5}	9.89·10^{-5}	9.79·10^{-5}	9.67·10^{-5}
D_k/m^2 s^{-1}	4.32·10^{-6}	4.20·10^{-6}	4.07·10^{-6}	3.93·10^{-6}
D_{eff}/m^2 s^{-1}	1.90·10^{-7}	1.85·10^{-7}	1.80·10^{-7}	1.74·10^{-7}

the factor ε/q accounts for the influence of morphology of the porous catalyst extrudate, where ε is the porosity, and q is the porous tortuosity of the catalyst particle.

For the assessment of the molecular diffusion coefficient D_{ij}, the Hirschfelder correlation was used [41]:

$$D_{ij} = \frac{0,001858.T^{1,5}\left[\left(M_i + M_j\right)/M_iM_j\right]^{0,5}}{p^2\sigma_{ij}^2\Omega_{ij}} \tag{4}$$

where j – component of gas mixture; T – temperature, K; M_i, M_{N2O} – molar weight of i-compound, $i = $ N$_2$O, g mol^{-1}; Mj – molar weight of j-compound, j = N$_2$, O$_2$, g mol^{-1}; σ – the distance between two particles; p – pressure, Pa; Ω is the collision integral, tabulated elsewhere [42].

To determine the molecular diffusivity (D_m) of N$_2$O in a multi-component mixture we applied the Wilke correlation, which takes into account the reaction stoichiometry and concentration of each gas component (y_j):

$$D_m = \frac{1 - y_i}{\sum_{j=1}\frac{y_j}{D_{ij}}} \tag{5}$$

The Knudsen diffusion coefficient $D_{k,N2O}$, in turn, was calculated by means of the following equation:

$$D_{k,N_2O} = 97 \cdot r_o \cdot \sqrt{\frac{T}{M_{N_2O}}} \tag{6}$$

where r_o is catalyst pore radius, m.

The numerical values of all diffusion coefficients of interest for the selected temperatures of the deN$_2$O reaction are summarized in Table 4.

The resultant concentration profiles for the investigated catalyst extrudates were calculated according to [43,44]

$$\frac{C_{N_2O}}{C_{N_2O,s}} = \frac{r}{r_p}\frac{\sinh\left(\Phi \cdot {^r/_{r_p}}\right)}{\sinh(\Phi)} \tag{7}$$

where $C_{N2O,s}$ is the N$_2$O concentration at the external surface of the catalyst, C_{N2O} is N$_2$O concentration on the catalyst surface inside the extrudate.

The characteristic parameters of the Al$_2$O$_3$ support used in the calculations are summarized in Table 3. They are assumed to be representative for the supported catalysts as well. The values of the effectiveness factor and Thiele modulus are summarized in Table 5, for Im-N, Cm-N and Sp-NN catalysts, respectively. They represent three classes of the concentration profiles of the active phase radial distribution across the extrudate.

The profiles of the N$_2$O concentration across the Im-N, Cm-N and Sp-NN catalysts extrudates for 550 °C (where the catalysts exhibit the N$_2$O conversion in the range of 20 − 70%, Table 2) are plotted in Fig. 8. The zero point of the coordinate system in Fig. 8 refers to the center of the extrudate. As expected, in all cases, the N$_2$O concentration strongly decreases inside the extrudates, reaching zero at ~0.5 mm from the center.

Table 5
The Thiele modulus (Φ) and the effectiveness factor (η) for various temperatures of deN$_2$O reaction for the selected Im-N, Cm-N and Sp-NN catalysts.

Catalyst	T/°C	600	550	500	450
Im-N	Φ	4.364	2.724	1.598	0.870
	η	0.2291	0.3640	0.5766	0.8062
Cm-N	Φ	5.528	4.000	2.769	1.817
	η	0.1809	0.2498	0.3583	0.5221
Sp-NN	Φ	2.906	1.761	1.000	0.524
	η	0.3421	0.5352	0.7617	0.9175

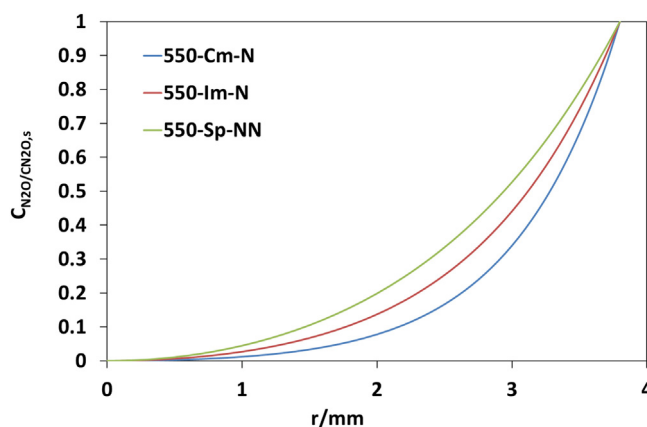**Fig. 8.** The calculated N$_2$O concentration profiles ($C_{N2O}/C_{N2O,s}$) across the catalyst extrudate for the Cm-N, Im-N and Sp-NN catalysts for 550 °C reaction temperature. The zero point of the coordinate system corresponds to the center of the pellet.
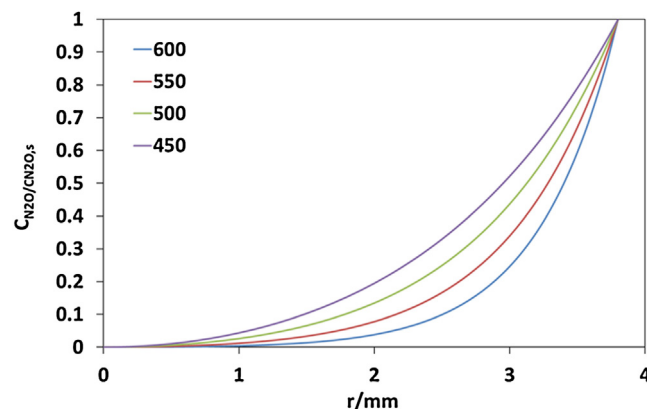

Fig. 9. The calculated N$_2$O concentration profiles ($C_{N2O}/C_{N2O,s}$) across the catalyst extrudate for the Cm-N sample for 450, 500, 550 and 600 °C reaction temperature. The zero point of the coordinate system corresponds to the center of the pellet.

For the most active Cm-N catalyst, where the sharpest decrease of the concentration profile is observed, the radial changes in the N$_2$O concentration were also calculated for different temperatures (Fig. 9). The increase of the reaction temperature from 450 to 600 °C leads to the increase in the reaction rate and consequently the N$_2$O concentration profile is distinctly more bent.

The calculated profiles were superimposed on the cross section of the Cm-N (Fig. 10a), Im-N (Fig. 10b) and Sp-NN (Fig. 10c) extrudates to illustrate the extent of the spinel active phase utilization for the N$_2$O decomposition. As a simple measure of this parameter,
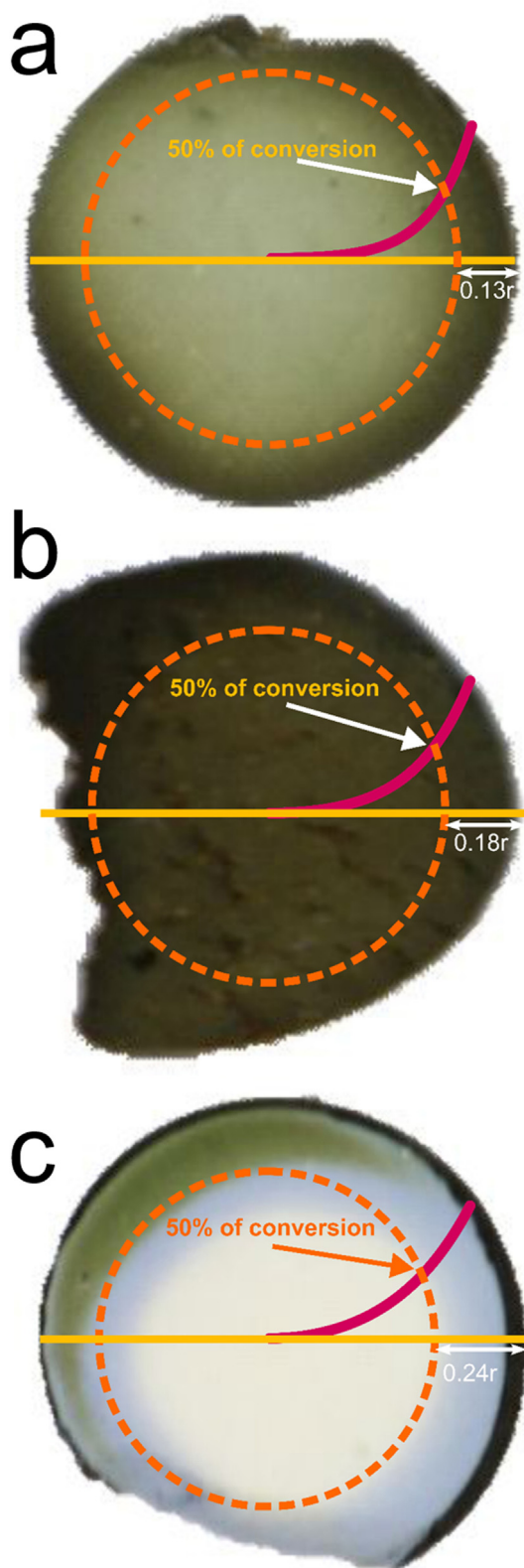
Fig. 10. Schematic representation of the N2O concentration profile (penetration depths) across the Cm-N (a), Im-N (b) and Sp-NN (c) catalyst extrudates. The dotted circle corresponds to 50% conversion of N2O, and the resultant $d_{50\%}$ distance is equal to 0.13r, 0.18r and 0.24r for Cm-N (a), Im-N (b) and Sp-NN (c), respectively.

we have calculated the distance from the extrudate surface to the point that corresponds to the 50% conversion of N$_2$O ($d_{50\%}$). This distance is equal to 0.13r, 0.18r and 0.24r for the Cm-N (Fig. 10a), Im-N (Fig. 10b) and Sp-NN (Fig. 10c) samples, respectively, where r is a radius of the extrude cross-section measured from the center to its external surface.

In the case of the most active sample (Cm-N), a good congruence of the conversion profile and the spinel repartition is observed, implying that an optimal dispersion of the catalyst active phase across the extrudate was successfully achieved. For the Im-N catalyst, the inspection of Fig. 10b shows clearly that a substantial part of the active phase will remain idle during the catalytic reaction. The opposite situation appears for the Sp-NN catalyst, where the Co$_3$O$_4$ shell is apparently too thin and the $d_{50\%}$ distance is dominated by the CoAl$_2$O$_4$ phase of poor activity.

Thus, the effectiveness factors can be directly related to activity only when the active phase is spread uniformly across the catalyst extrudate (Fig. 10b). In the case of a nonhomogeneous distribution, such as that observed in Fig. 10c penetration of the N$_2$O reactant into the center of the extrudate does not lead to the activity enhancement since in this region the spinel active phase is depleted. As a result, the highest conversion is expected for those catalysts where the overlap between the N$_2$O concentration and the active phase distribution profiles is maximal.

The obtained results have a straightforward practical impact for the development or the supported catalyst for the N$_2$O decomposition. The radial dispersions of the spinel active phase obtained in the presence by organic component (glycerol or urea) in the precursor mixture exhibit the optimal profiles with respect to utilization of the extrudate interior for the catalyzed reaction. Since the evaluated preparation methods are easily scalable they may be implemented on a larger (industrial) scale in a simple way.

4. Conclusions

The effect of the preparation method of the supported Co$_3$O$_4$|Al$_2$O$_3$ catalyst for N$_2$O decomposition on its performance was systematically examined. The following easily scalable methods for catalyst preparation were selected: impregnation with an aqueous solution of cobalt nitrate or chloride, impregnation with glycerol-assisted cobalt nitrate solution, combustion synthesis, spray with cobalt nitrate solution, and spray method with Co(NO$_3$)$_2$ with extrudates soaked in NH$_3$. The relation between active phase nature, dispersion and catalytic activity was revealed by means of XRF, XRD, μ-RS, UV–vis, SEM/TEM/EDX and the TPSR catalytic tests. The comparison of the calculated concentration profiles of N$_2$O across the extrudates with the radial distribution of the active phase and the spinel particle size and its chemical nature (Co$_3$O$_4$ versus CoAl$_2$O$_4$) allowed for straightforward rationalization of the obtained results and selection of the optimal preparation method. It was shown that among the investigated methods, the catalysts synthesized in the presence of organic component in the precursor mixture (glycerol or urea) exhibit the active phase distribution that complies with the intraparticle diffusion of N$_2$O in the most congruent way.

Appendix A. Supplementary data

Supplementary data associated with this article can be found, in the online version, at http://dx.doi.org/10.1016/j.apcatb.2017.03.053.

References

[1] J. Pérez-Ramírez, F. Kapteijn, K. Schöffel, J.A. Moulijn, Appl. Catal. B 44 (2003) 117.
[2] G. Grzybek, P. Stelmachowski, S. Gudyka, P. Indyka, Z. Sojka, N. Guillén-Hurtado, V. Rico-Pérez, A. Bueno-López, A. Kotarba, Appl. Catal. B 180 (2016) 622.
[3] P. Stelmachowski, F. Zasada, W. Piskorz, A. Kotarba, J.F. Paul, Z. Sojka, Catal. Today 137 (2008) 423.
[4] B.M. Abu-Zied, S.M. Bawaked, S.A. Kosa, W. Schwieger, Catalysts 6 (5) (2016) 70.
[5] M. Konsolakis, ACS Catal. 5 (11) (2015) 6397.
[6] P. Esteves, Y. Wu, C. Dujardin, M.K. Dongare, P. Granger, Catal. Today 176 (2011) 453.
[7] F. Zasada, P. Stelmachowski, G. Maniak, F. Paul, A. Kotarba, Z. Sojka, Catal. Lett. 127 (2009) 126.
[8] B.M. Abu-Zied, S.A. Soliman, S.E. Abdellah, J. Chin. Catal. 35 (2014) 1105.
[9] P. Stelmachowski, K. Ciura, G. Grzybek, Catal. Sci. Technol. 6 (2016) 5554.
[10] Y. Wu, C. Dujardin, C. Lancelot, J.P. Dacquin, V.I. Parvulescu, M. Cabié, C.R. Henry, T. Neisius, P. Granger, J. Catal. 328 (2015) 236.
[11] Y. Wu, X. Ni, A. Beaurain, C. Dujardin, P. Granger, Appl. Catal. B 125 (2012) 149.
[12] Y. Wu, C. Cordier, E. Berrier, N. Nuns, C. Dujardin, P. Granger, Appl. Catal. B 140–141 (2013) 151.
[13] M. Rutkowska, Z. Piwowarska, E. Micek, L. Chmielarz, Microporous Mesoporous Mat. 209 (2015) 54.
[14] D. Pietrogiacomi, M.C. Campa, L.R. Carbone, S. Tuti, M. Occhiuzzi, Appl. Catal. B 187 (2016) 218.
[15] M. Zabilskiy, P. Djinovic, E. Tchernychova, A. Pintar, Appl. Catal. B 197 (2016) 146.
[16] S. Parres-Esclapez, M.J. Illán-Gómez, C. Salinas-Martínez de Lecea, A. Bueno-López, Int. J. Greenhouse Gas Control 11 (2012) 251.
[17] S. Gudyka, G. Grzybek, J. Gryboś, P. Indyka, B. Leszczyński, A. Kotarba, Z. Sojka, Appl. Catal. B 201 (2017) 339.
[18] S. Storsæter, B. Tøtdal, J.C. Walmsley, B.S. Tanem, A. Holmen, J. Catal. 236 (2005) 139.
[19] J.A. Gómez-Cuaspud, M. Schmal, Appl. Catal. B 1–10 (2014) 148.
[20] G. Saracco, S. Specchia, V. Specchia, Chem. Eng. Sci. 51 (1996) 5289.
[21] K. Klaigaew, C. Samart, C. Chaiya, Y. Yoneyama, N. Tsubaki, P. Reubroycharoen, Chem. Eng. J. 278 (2015) 166.
[22] L.D. Vella, S. Specchia, Catal. Today 176 (2011) 340.
[23] M. Minnermann, H.K. Grossmann, S. Pokhrel, K. Thiel, H. Hagelin-Weaver, M. Bäumer, L. Mädler, Catal. Today 214 (2013) 90.
[24] S. Specchia, C. Galletti, V. Specchia, Stud. Surf. Sci. Catal. 175 (2010) 59.
[25] G. Ercolino, G. Grzybek, P. Stelmachowski, S. Specchia, A. Kotarba, V. Specchia, Catal. Today 257 (2015) 66.
[26] G. Ercolino, P. Stelmachowski, G. Grzybek, A. Kotarba, S. Specchia, Appl. Catal. B 206 (2017) 712.
[27] L. Lutterotti, S. Matthies, H.R. Wenk, A.J. Schultz, J. Richardson, J. Appl. Phys. 81 (1997) 594.
[28] EUROKIN spreadsheet on requirements for measurement of intrinsic kinetics in the gas-solid fixed-bed reactor, (2012), www.eurokin.org.
[29] G.F. Froment, K.B. Bischoff, Chemical Reactor Analysis and Design, Wiley, 1979, pp. 617.
[30] J. Zielinski, React. Kinet. Catal. Lett. 17 (1981) 69.
[31] Y. Wei, K.W. Nam, K.B. Kim, G. Chen, Solid State Ionics 177 (2006) 29.
[32] L.V. Gasparov, D.B. Tanner, D.B. Romero, H. Berger, G. Margaritondo, L. Forro, Phys. Rev. B 62 (2000) 7939.
[33] Z.H. Zhou, J.M. Xue, J. Wang, H.S.O. Chan, T. Yu, Z.X. Shen, J. Appl. Phys. 91 (2002) 6015.
[34] P. Stelmachowski, G. Maniak, J. Kaczmarczyk, F. Zasada, W. Piskorz, A. Kotarba, Z. Sojka, Appl. Catal. B 146 (2014) 105.
[35] C.S. Cheng, M. Serizawa, H. Sakata, T. Hirayama, Mater. Chem. Phys. 53 (1998) 225.
[36] H. Keppler, N. Bagdassarov, Chem. Geol. 158 (1999) 105.
[37] K.J. Kim, Y.R. Park, Solid State Commun. 127 (2003) 25.
[38] D. Rangappa, T. Naka, A. Kondo, M. Ishii, T. Kobayashi, T. Adschiri, J. Am. Chem. Soc. 129 (2007) 11061.
[39] C.C. Yang, S. Li, J. Phys. Chem. B 112 (2008) 14193.
[40] O.N. Shebanova, P. Lazor, J. Raman, Spectroscopy 34 (2003) 845.
[41] J. Thullie, M. Bodzek, Inż. Ap. Chem. 42 (4) (2003) 12.
[42] S. Bretsznajder, Właściwości gazów i cieczy, (1962), WNT, Warszawa.
[43] H.S. Fogler, Elements of Chemical Reaction Engineering, 3th ed., Prentice Hall PTR, New Jersey, 1999.
[44] L. Obalova, K. Jiratova, K. Karaskova, F. Kovanda, Chin. J. Catal. 32 (2011) 816.